3D-cross Nanowire Networks Recover Full Terahertz State

Authors: Kun Peng[1], Dimitars Jevtics[2], Fanlu Zhang[3], Sabrina Sterzl[1], Djamshid A Damry[1], Mathias U Rothmann[1], Benoit Guilhabert[2], Michael J Strain[2], Hark H Tan[3], Laura M Herz[1], Lan Fu[3], Martin D Dawson[2], Antonio Hurtado[2], Chennupati Jagadish[3], Michael B Johnston[1]*

Affiliations:

[1]Department of Physics, University of Oxford, Clarendon Laboratory, Oxford, OX1 3PU, United Kingdom.

[2]Institute of Photonics, SUPA Department of Physics, University of Strathclyde, Technology and Innovation Centre, 99 George Street, G1 1RD, Glasgow, United Kingdom.

[3]Department of Electronic Materials Engineering, Research School of Physics, The Australian National University, Canberra, ACT 2601, Australia.

*Correspondence to: michael.johnston@physics.ox.ac.uk

Abstract:

Terahertz radiation encompasses a wide band of the electromagnetic spectrum spanning from microwaves to infrared light, and is a particularly powerful tool for both fundamental scientific research and applications such as security screening, communications, quality control and medical imaging. Considerable information can be conveyed by the full polarization state of terahertz light, yet to date most time-domain terahertz detectors are sensitive to just one polarization component. Here we demonstrate a nanotechnology-based semiconductor detector utilizing cross-nanowire networks that records the full polarization state of terahertz pulses. The monolithic device allows simultaneous measurements of the orthogonal components of the THz electric field vector without crosstalk. Furthermore, we demonstrate the capabilities of the detector for the study of metamaterials.

One Sentence Summary:

Antenna-coupled 3D-cross nanowire networks enable fast and precise detection of the full polarization state of terahertz pulses.

Main Text:

The terahertz (THz) band (0.1 to 30 THz) of the electromagnetic spectrum is where electronics meets optics, with THz photons sharing properties from the neighbouring spectral regions. For example, in common with microwaves, THz radiation is non-ionizing and penetrates through most non-conducting materials, yet THz radiation can be directed by optical components similar to infrared light. This mixed property enables a wide variety of THz applications including wireless communication, spectroscopy, sensing and imaging (*1*).

Time-domain spectroscopy (TDS) with single or sub-cycle pulses of THz radiation is a powerful tool for materials characterization (*2*), since it directly measures both the amplitude E(ω) and phase ϕ(ω) of electromagnetic radiation over a broad range of frequencies, ω, thereby allowing straightforward extraction of a material's complex dielectric properties. The pulsed nature of the technique also allows tomographic 3D spatial mapping of dielectric properties of materials using a methodology similar to radar. Such spectral imaging is non-destructive and has been applied in a wide range of applications including pharmaceutical quality control, medical diagnostics and production-line inspection. Furthermore, the pulsed nature of the TDS technique facilitates studying dynamic processes in materials with femtosecond time resolution (*3, 4*).

The vast majority of THz-TDS systems are based on generation and detection of a linearly polarized component of single-cycle THz pulses. In the frequency domain such data may be represented as $E(\omega)e^{i\phi(\omega)}$, where the two parameters $E(\omega)$ and $\phi(\omega)$ are the amplitude and phase spectra respectively. Yet a complete description of a THz pulse must also specify its polarization, which requires two additional parameters to describe the frequency dependence of polarization angle and ellipticity. So formally the full state of a THz pulse may be described by a four-dimensional Stokes vector or Jones vector for each frequency component of its broad spectrum (*5*). Thus, by encoding polarization information on a THz pulse it is theoretically possible to double the information it transmits. In spectroscopy, measuring the full state of THz radiation facilitates extraction of anisotropic dielectric properties of materials (which could be affected by surface topography, crystal structure, stress and magnetic fields), and is key to new techniques such as THz optical-Hall effect *(6)*, THz ellipsometry *(7)* and vibrational circular dichroism spectroscopy *(8)*. In THz pulsed imaging applications, polarization information enables high-resolution THz tomography and helps correct the artefacts associated with birefringence and scattering from sample edges *(9)*. Therefore, the capability of polarization measurement with THz-TDS is in high demand. In fact, polarization-resolved THz-TDS systems have been demonstrated since the late 1990s *(10)*. However, a lack of measurement schemes for fast and precise polarization sensing has impeded their applications. Currently, polarization detection with THz-TDS can be realized using wire-grid THz polarizers, rotatable polarized THz sources *(11, 12)*, or polarization-sensitive detectors *(13, 14)*.

In most cases, only one component of the THz electric field vector can be measured over one time-domain scan. For determining the full polarization state, doubled data acquisition time is required, which is problematic for mapping/imaging applications. Utilization of a multi-contact photoconductive antenna (*15-17*) for polarization-sensitive measurement is an exceptional case, since this detector type is capable of simultaneously measuring the THz electric field vector along multiple directions during a single time-domain scan. However, these devices are difficult to align and crosstalk between detection channels complicates extraction of the polarization state (*15, 18*), thereby limiting their practical use. Seemingly, the field has reached a technological plateau, calling for a new approach. In this report, we propose and demonstrate a novel detector design that utilizes nanotechnology to measure THz polarization in full. The detector is alignment-insensitive and free from the crosstalk, suggesting an ease of implementation in both scientific and industrial settings.

The active elements in our detector are single-crystal semiconductor nanowires that have been systemically studied in our previous work (*19-21*) confirming their good suitability for photoconductive THz detection. Here we utilized indium phosphide (InP) nanowires with a pure wurtzite crystal structure and an approximate average diameter and length of 280 nm and 10 μm respectively (see MM1). The detector architecture is shown in Fig.1 and consists of two orthogonal gold bow-tie electrodes that are separately bridged by well-aligned nanowires in a 'hashtag' configuration. The nanowires on each bow-tie electrode are parallel to the gap orientation, and thus the nanowires contacted by different bow-tie electrodes are orthogonal while being spatially separated perpendicular to the substrate to ensure they are electrically isolated.

The device architecture was inspired by our previous findings that both single semiconductor nanowires (*22*) and bow-tie THz detectors exhibit extremely high polarization selectivity to absorption of both THz radiation and above-bandgap light. Thus bow-tie THz detectors based on orthogonal semiconductor nanowires should offer little electromagnetic interference between polarization channels, making them perfect for full polarization characterization.

The cross-nanowire devices were realized through two steps of electron beam lithography and nanowire micropositioning using a 'Transfer Print' technique to effectively manipulate the nanowire location and orientation in device (see MM2 and MM3), enabling the creation of electrically isolated orthogonal polarization detection channels, thereby avoiding electrical crosstalk. In this work we concentrate on a 'hashtag' device design with a pair of nanowires per channel, however the numbers of nanowires for each electrode can be altered, for example a crossed-single-nanowire structure is presented in the Fig.S3.

After fabrication, the polarization-sensitive-cross-nanowire detectors were characterized in a custom-built THz-TDS system (see MM4 and MM5). Briefly, each near-infrared pulse from a femtosecond laser was split into two: one used to generate a linearly polarized THz pulse in a THz emitter and the other to photoexcite electrons and holes in the cross-nanowire detector. The THz pulse from the emitter was focused on the detector inducing a transient photocurrent (proportional to the THz field) in each detection channel, which was recorded as a function of time delay t between the THz pulse and optical pulse. The electric-field component of the THz pulse polarized parallel to each antenna (electrode) caused current to flow along its nanowires only after photoexcitation (*23*). Thus to recover the electric field of the THz pulse in the time domain, the photocurrent data for each channel were differentiated as a function of t (see ST1) (*24*). Frequency-domain data were obtained by Fourier transform of the time-domain data.

Firstly, the spectral response of our nanowire detector was examined as shown in Fig.2A. It can be seen clearly that the horizontal and vertical channels produced responses simultaneously with a current level of a few picoamps, spectral bandwidth of ~2 THz (defined as the cut-off frequency at the noise floor of the frequency spectrum) and low-noise performance, which are consistent with our earlier work (*20*). The current generated by the 'hashtag' detector is limited by the nanosized active material volume but can be increased by adding more nanowires to the array or using larger diameter nanowires. The two orthogonal channels have a strong linear response relative to the incident THz polarization, where the response current reaches to a maximum when the THz pulse is polarized parallel to the channel orientation and drops to nearly zero when polarized perpendicular to the channel orientation.

Finite-difference-time-domain simulations (FDTD) were performed to examine the electrode response to the incident THz polarization, which is also linear for each bow-tie structure (see Fig.2A). The bow-tie antenna structure enhances the intrinsic THz-polarization

sensitivity of the nanowires and collects the THz electric field over a much larger area (and concentrates it at the antenna center). Fig.2B illustrates more detailed angle-dependence responses (peak-to-peak current) of both orthogonal detection channels relative to the THz polarization, in excellent agreement with expected cosine and sine functions. This indicates that the two orthogonal channels are independent without any measurable crosstalk between them.

For comparison, we fabricated a multi-contact photoconductive antenna, which had the same electrode structure as used in our nanowire detector but utilizing a more conventional Fe^{+}-implanted InP substrate as the active material. This bulk reference device was measured under identical conditions to the nanowire detector. As expected, strong crosstalk dominates the signal and furthermore the degree of crosstalk is dependent on the size and position of the optical excitation spot (see ST3), making extraction of the THz polarization state non-trivial and alignment-dependent.

The polarization selectivity of each channel of the nanowire 'hashtag' detector was assessed by measuring the cross-polarized THz extinction ratio. This ratio was found to be 2500 (in power) for the horizontal channel (1440 for the vertical channel), which is a significant improvement over the ratio of 256 in Ref (*16*) and 108 reported in Ref (*17*) (further analysis is provided in ST3). The high extinction ratio achieved by our 'hashtag' detector is expected as the aligned nanowires used in our detector are intrinsically polarization-sensitive and crosstalk-free. After the calibration (see ST4), we assessed the detector sensitivity to the change of the incident THz polarization angle as shown in Fig.2C. The standard deviation of the measured angle values (calculated from the two-channel data) is 0.38°, indicating the minimum detectable change of polarization angle is less than 0.4° for our nanowire detector.

To demonstrate the versatility of a polarization-resolved THz-TDS system equipped by our nanowire detector, we characterized a THz metamaterial. Metamaterials for the THz band have attracted considerable attention because of their simplicity of design and capability of manipulating the polarization state of THz radiation (*25*), which is difficult to achieve in natural materials. Here we studied a metamaterial (twisted split-ring resonator pair) that functions as a polarization converter. The schematic illustration of our measurement is shown in Fig.3A, and the morphology of the metamaterial is presented in Fig.3B (see MM7). When a linearly-polarized THz pulse is transmitted through the metamaterial, a coupling effect will induce co- and cross-polarization components in the transmission direction. FDTD simulations were performed to examine the coupling effect for comparison with experimental results. The simulated and transmission amplitude spectra measured with the 'hashtag' detector are compared in Fig.3C and show excellent agreement. In particular, the co-polarized transmission has a resonance splitting feature (at 1.06 and 1.4 THz) that is also observed in the measured spectra. The difference in the transmission ratio could be attributed to imperfect experimental conditions and/or the dielectric properties of the materials being slightly different from the values used in the simulation. A measurement on similar metamaterial type has been reported (*26*), where four wire-grid THz polarizers were employed in the system. Our system just required a single scan while providing high polarization accuracy.

In summary, orthogonally-crossed nanowire networks were utilized to develop an ultrafast detector capable for recording the full polarization state of THz radiation and its capabilities were demonstrated in the characterization of metamaterials. The monolithic 'hashtag' device is compact and can immediately replace conventional photoconductive receivers in most THz-TDS spectrometers and imaging systems, without any change to the optical layout while vastly improving the capabilities of such systems by including additional spectral polarization information without increased acquisition time. The detector architecture

is simple and universal, so any quasi-1D semiconductor nanostructures (e.g. nanorods and nanopillars) could be exploited for further optimization of device performance, in terms of signal-to-noise and accessing ultrabroad spectral bandwidth, thus paving the way to high-speed high-accuracy THz pulsed imaging. Fast parallel data acquisition for far-field spectral imaging could also be achieved by forming arrays of the 'hashtag' detectors. Furthermore, the detector concept could be scaled down as sub-wavelength detection units in near-field THz imaging systems for polarization-based super resolution (i.e. nanoscale spatial resolution), or use as an on-chip THz-TDS spectrometer. Therefore, the capabilities and geometry of the detector and its associated on-chip technologies opens up a wide range of new scientific applications spanning physics, biology, chemistry, and engineering, while potentially enabling new approaches to industrial quality control, security imaging and high-speed communications.

References and Notes: (1-26 for main text, 27-29 for supplementary materials)

1. S. Dhillon *et al.*, *Journal of Physics D: Applied Physics* **50**, 043001 (2017).
2. B. Ferguson, X. C. Zhang, *Nature Materials* **1**, 26-33 (2002).
3. C. Riek *et al.*, *Science* **350**, 420-423 (2015).
4. S. Schlauderer *et al.*, *Nature* **569**, 383-387 (2019).
5. E. Castro-Camus, M. B. Johnston, *Journal of Optics A: Pure and Applied Optics* **11**, 105206 (2009).
6. D. M. Mittleman, J. Cunningham, M. C. Nuss, M. Geva, *Applied Physics Letters* **71**, 16-18 (1997).
7. K. N. Okada *et al.*, *Nature Communications* **7**, 12245 (2016).
8. W. Choi *et al.*, *Nature Materials* **18**, 820-826 (2019).
9. S. Watanabe, *Photonics* **5**, 58 (2018).
10. B. B. Hu, M. C. Nuss, *Optics Letters* **20**, 1716-1718 (1995).
11. Q. Chen, X. C. Zhang, *Applied Physics Letters* **74**, 3435-3437 (1999).
12. C. D. W. Mosley, M. Failla, D. Prabhakaran, J. Lloyd-Hughes, *Scientific Reports* **7**, 12337 (2017).
13. E. Castro-Camus *et al.*, *Optics Express* **15**, 7047-7057 (2007).
14. N. Nemoto, T. Higuchi, N. Kanda, K. Konishi, M. Kuwata-Gonokami, *Optics Express* **22**, 17915-17929 (2014).
15. D. S. Bulgarevich *et al.*, *Optics Express* **22**, 10332-10340 (2014).
16. A. Hussain, S. R. Andrews, *Optics Express* **16**, 7251-7257 (2008).
17. E. Castro-Camus *et al.*, *Applied Physics Letters* **86**, 254102 (2005).
18. G. Niehues *et al.*, *Optics Express* **23**, 16184-16195 (2015).
19. K. Peng *et al.*, *Nanotechnology* **28**, 125202 (2017).
20. K. Peng *et al.*, *Nano Letters* **16**, 4925-4931 (2016).
21. K. Peng *et al.*, *Nano Letters* **15**, 206-210 (2015).
22. S. A. Baig *et al.*, *Nano Letters* **17**, 2603-2610 (2017).
23. Z. Yang *et al.*, *Science* **365**, 1017-1020 (2019).
24. E. Castro-Camus *et al.*, *Journal of Applied Physics* **104**, 053113 (2008).
25. T. J. Yen *et al.*, *Science* **303**, 1494-1496 (2004).
26. C. Y. Li, C. C. Chang, Q. L. Zhou, C. L. Zhang, H. T. Chen, *Optics Express* **25**, 25842-25852 (2017).
27. Q. Gao *et al.*, *Nano Letters* **14**, 5206-5211 (2014).
28. H. J. Joyce, J. L. Boland, C. L. Davies, S. A. Baig, M. B. Johnston, *Semiconductor Science and Technology* **31**, 103003 (2016).
29. B. Guilhabert *et al.*, *ACS Nano* **10**, 3951-3958 (2016).

Acknowledgments: We thank Junjie Liu, Xinya Bian, Paul Pattinson, Patrick Parkinson and Marco Zerbini for useful discussion. We acknowledge the Australian National Fabrication Facility, ACT node (ANFF-ACT) for access to the facilities. Thanks to Ziyuan Li's arrangement, simulation was undertaken with the assistance of resources from the National Computational Infrastructure (NCI Australia). **Funding:** This work was supported by EPSRC(UK), ARC(Australia) and the European Union's Horizon 2020 research and innovation program under grant agreements 735008 (SiLAS) and 828841 (ChipAI). **Author contributions:** MBJ conceived the device concept. MBJ, CJ and LF established this project. KP worked on device design, fabrication, characterization and simulation. DJ, BG, MJS, MDD and AH developed the transfer printing technique for the integration of nanowires. DJ performed the transfer-print process under the supervision of AH. FZ, LF and HHT created the nanowires and ion-implanted wafers. SS characterized nanowire photoconductivity. DAD assisted with the fabrication and system optimization. MUR performed SEM under the supervision of LMH. KP and MBJ prepared the manuscript. All authors discussed and commented on the manuscript. **Competing interests:** Oxford University has filed a patent on the detector concept. **Data and materials availability:** All data is available in the main text or the supplementary materials. The data used to create the plots in this report are available in Oxford University Research Archive.

Supplementary Materials:

Materials and Methods (1-7)

Supplementary Text (1-7)

Figures S1-S13

References (27-29)

Fig. 1. Structure of polarization-sensitive-cross-nanowire THz detector. (A) Schematic illustration of device geometry. **(B)** SEM image of the as-grown InP nanowire array. **(C)-(E)** SEM images of the fabricated detector (blue: entire device; green: center of device; orange: close-up center of device under a tilted view of 25°).

Fig. 2. Characterization of polarization-sensitive-cross-nanowire detector in THz-TDS. (A) Responses of the nanowire detector relative to the incident THz polarization (left: raw and processed time-domain THz electric field; middle: amplitude and phase spectrum of the THz electric field; right: simulated THz electric field distribution at 1 THz). 0°, 30°, 60° and 90° are the angles that the incident THz pulse is polarized at. Red solid line: response from the horizontal-detection channel. Blue solid line: response from the vertical-detection channel. **(B)** Relationship between the two orthogonal detection channels in the nanowire detector as a function of the incident THz polarization. Red dots: response from the horizontal-detection channel. Blue circles: response from the vertical-detection channel. **(C)** Relative changes of the THz polarization measured by the nanowire detector (cross-circles) for different emitter rotation angle.

Fig. 3. Application demonstration of polarization-sensitive-cross-nanowire detector. (A) Schematic representation of transmission measurement of a THz metamaterial. The arrowed blue solid lines show the polarization of the THz pulse before and after passing through the metamaterial. **(B)** SEM images of the fabricated metamaterial. **(C)** Simulated and measured transmission spectra of the THz metamaterial in co- (solid line) and cross- (dot line)

polarizations. Shadow is the error bar showing the standard variation of repeats in the same measurement.

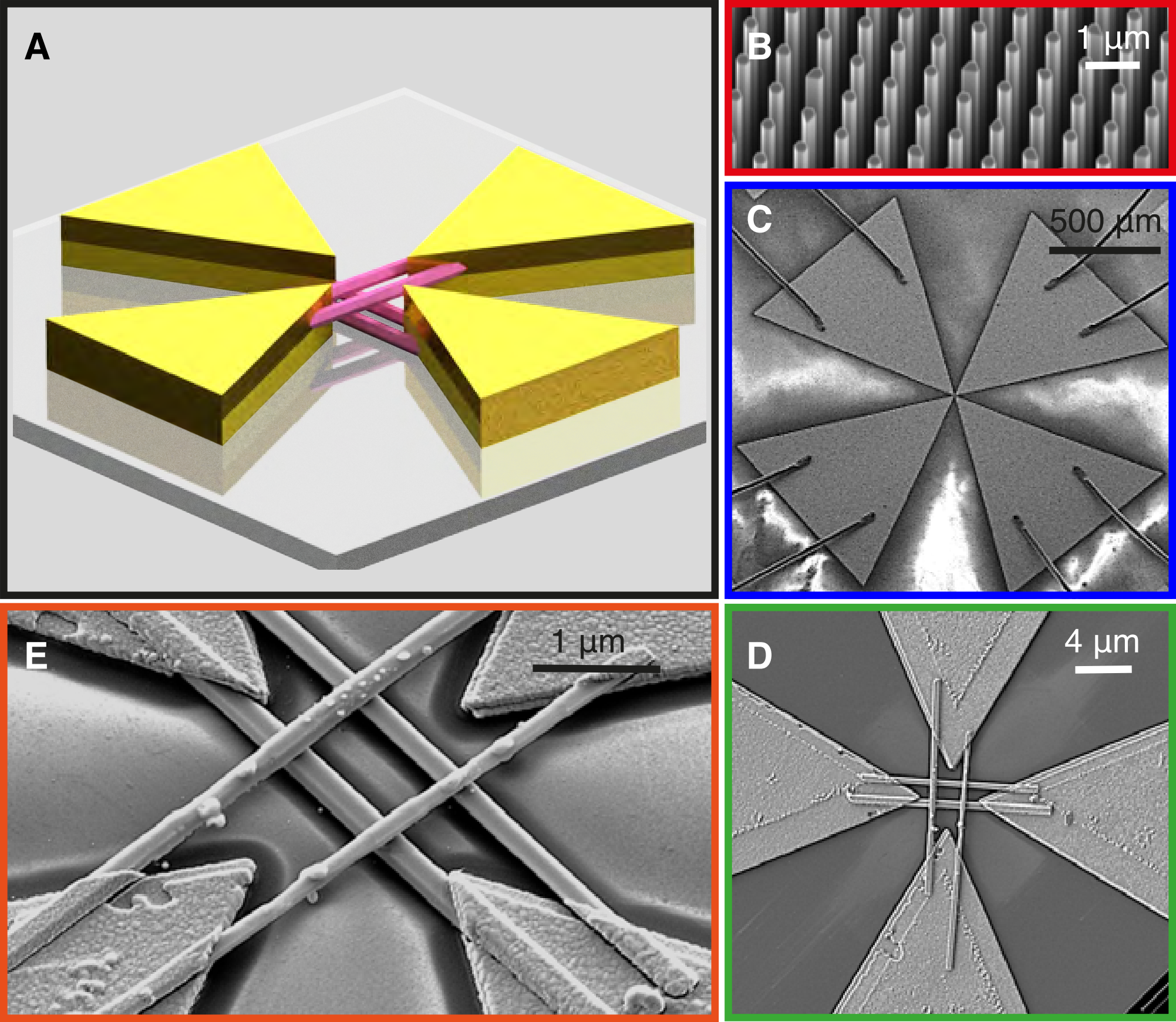
A
B
1 µm
C
500 µm
E
1 µm
D
4 µm

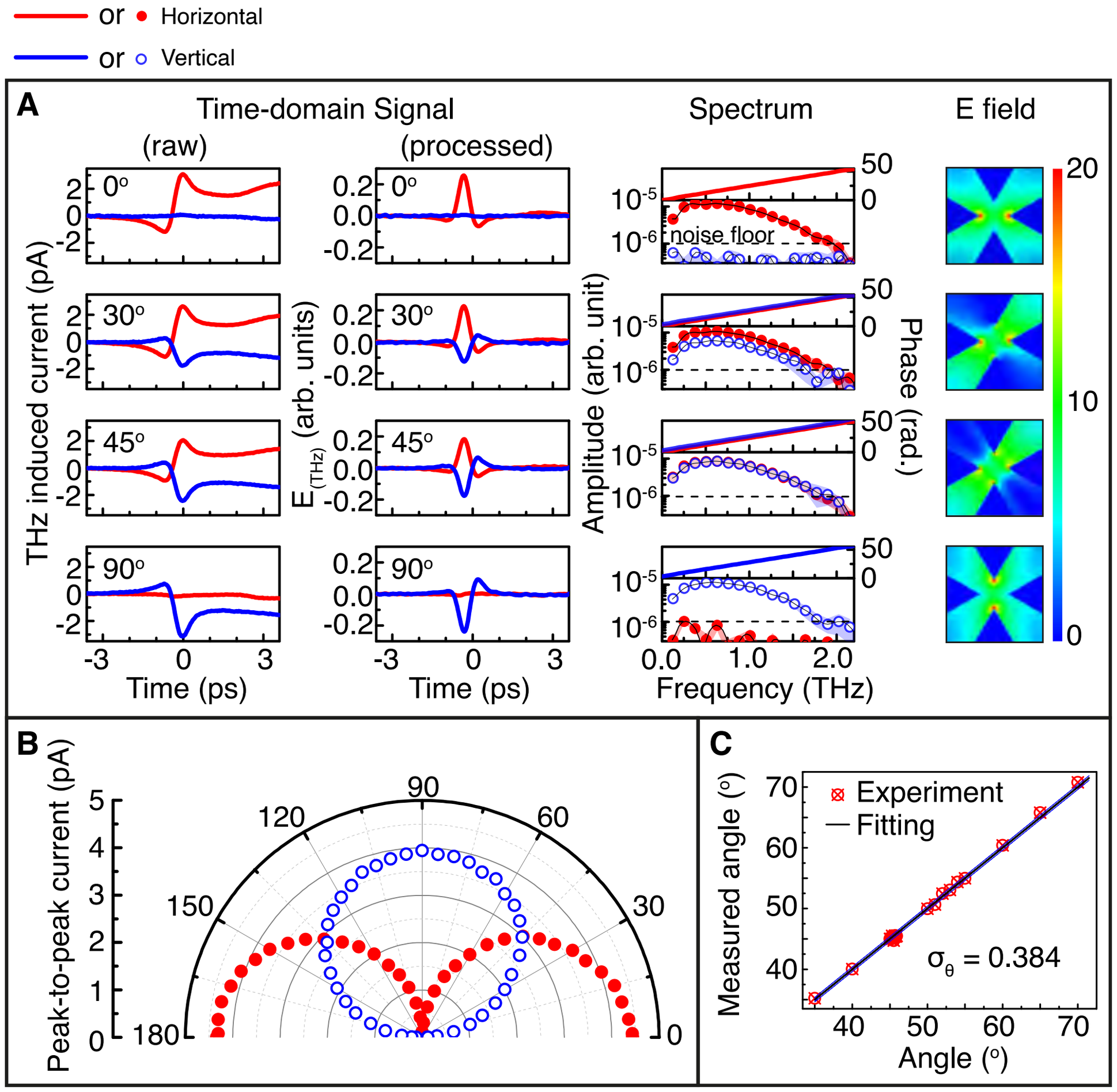
or Horizontal
or Vertical
A
Time-domain Signal
(raw)
(processed)
Spectrum
E field
0°
30°
45°
90°
THz induced current (pA)
E(THz) (arb. units)
Amplitude (arb. unit)
Phase (rad.)
noise floor
Time (ps)
Frequency (THz)
B
Peak-to-peak current (pA)
C
Measured angle (°)
Experiment
Fitting
σθ = 0.384
Angle (°)

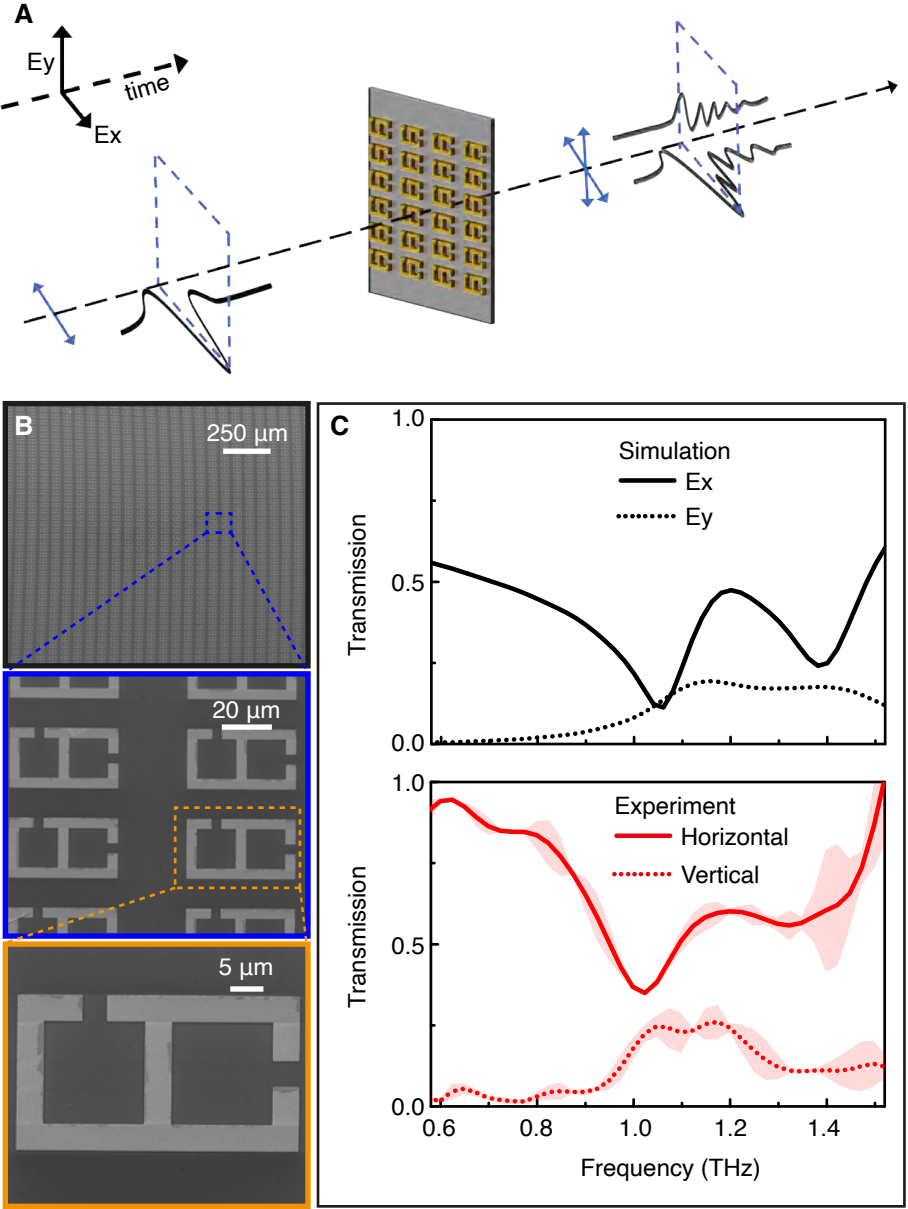
A
Ey
time
Ex
B
250 μm
20 μm
5 μm
C
Simulation
Ex
Ey
Transmission
1.0
0.5
0.0
Experiment
Horizontal
Vertical
Transmission
1.0
0.5
0.0
0.6
0.8
1.0
1.2
1.4
Frequency (THz)

Supplementary Materials for

3D-cross Nanowire Networks Recover Full Terahertz State

Kun Peng, Dimitars Jevtics, Fanlu Zhang, Sabrina Sterzl, Djamshid A Damry, Mathias U Rothmann, Benoit Guilhabert, Michael J Strain, Hark Hoe Tan, Laura M Herz, Lan Fu, Martin D Dawson, Antonio Hurtado, Chennupati Jagadish, Michael B Johnston*

*correspondence to: michael.johnston@physics.ox.ac.uk

This PDF file includes:

Materials and Methods

MM1. Nanowire growth and characterization

The indium phosphide (InP) nanowires were grown via catalyst-free selective-area metal-organic vapor phase epitaxy (SA-MOVPE). A 30-nm SiO_2 mask layer was firstly deposited on (111)A InP substrates, then patterned by electron beam lithography (EBL) to create arrays of circles. The circles were then transferred to the SiO_2 mask by wet chemical etching using buffered hydrogen fluoride solution. After etching, the diameter of the circles was 200 nm with a pitch of 800 nm. The patterned substrates were then loaded into a horizontal-flow low-pressure (100 mbar) MOVPE system (Aixtron 200/4). All samples were annealed at 750 °C for 10 min under a phosphine protective flow and grown at 730 °C for 40 min with trimethylindium and phosphine at a flow rate of 6.1×10^{-6} and 4.9×10^{-4} mol/min, respectively. Similar growth conditions have been previously reported elsewhere (*27*) and shown to produce pure wurtzite structurally uniform and high quantum efficiency InP nanowires with a range of diameters from 250 to 300 nm and lengths from 8 to 11 μm. Fig.S1A shows typical morphology profiles of the InP nanowires used in this work.

The photoconductivity of the InP nanowires were characterized via optical-pump/terahertz-probe (OPTP) spectroscopy. Details of the OPTP technique are depicted in Ref (*28*). The photoconductivity lifetime of the active material in the THz photoconductive detector determines the detector operation type and thus the signal processing technique. Fig.S1B presents the photoconductivity rise time (sub-picosecond) and photoconductivity lifetime (~ 970 ps) of an ensemble of the InP nanowires measured in this work, indicating the InP nanowire detectors are of integrating type (*24*). The carrier mobility of the InP nanowires was measured to be 606 ± 34 $cm^2\ V^{-1}\ s^{-1}$, which suggested that they would be suitable as nanowire photodetectors.

MM2. Nanowire device fabrication

The polarization-sensitive-cross-nanowire terahertz (THz) detector has a 3D device geometry as shown in Fig.1 (main text). In order to make the two orthogonal detection channels electrically isolated in one device, we proposed a fabrication scheme involving two cycles of electron beam lithography (EBL), nanowire transfer-printing and metal deposition, as shown in Fig.S2.

Firstly, a *z*-cut quartz substrate with gold markers was prepared using EBL. Then the InP nanowires were mechanically broken off from the as-grown substrate and positioned at a predefined location on the quartz substrate with designated orientation. Subsequently the *z*-cut quartz with the transferred nanowires was patterned by EBL to fabricate the electrodes. An oxygen plasma etch was then employed to further remove the resist residue on the nanowires, followed by a 9.3 % HCl chemical etching to remove the native oxide layer formed on the nanowire surface. Finally, the detector structure was metallized using thermal evaporation and lift-off, with Cr/Au (10 nm/330 nm) contacts. Up to now, the first half of the final device structure was completed with one of the two channels in the device being bridged by the nanowires. Next, fresh InP nanowires were positioned on the top surface of the electrodes (made during the previous fabrication stage), aligned with a direction orthogonal to that of the first set of transfer-printed nanowires. Afterwards the whole device sample was again patterned by EBL, etched and metalized,

following all the steps and recipes as described above, to create the two orthogonal nanowire-bridged channels. Since the average nanowire diameter was around 280 nm that was smaller than the 340 nm thickness of the deposited electrodes, the heights of first and second sets of transferred nanowires were different (the former are laid on the substrate and the latter are suspended from the substrate), forming an air gap of a few tens of nanometers in between. Therefore, the active materials (nanowires) in the two orthogonal channels were separated in the direction orthogonal to the plane of the substrate and hence did not touch. Thus the two detection channels were electrically isolated from each other. The numbers of nanowires for each channel could be manipulated as shown in Fig.S3.

MM3. Nanoscale transfer printing technique

InP nanowires were integrated in the THz detectors by means of nanoscale Transfer Printing (nano-TP). This technique uses polymeric (polydimethylsiloxane, PDMS) micron-size stamps (μ-stamps) to controllably capture individually-selected nanowires from their original substrate for their subsequent release at specific target locations into desired surfaces with very high positioning accuracy. For full details on the working mechanism and performance of nano-TP see (*29*).

Prior to starting the nano-TP processes, InP nanowires were mechanically transferred en masse from their growth substrate and dispersed onto a PDMS surface. After this preliminary step, the nanowires were visually inspected (using the microscope imaging system included in the nano-TP module) to select suitable nanowire dimensions for their integration into the THz detectors. Specifically, nanowires with longer lengths, clearly exceeding that of the gap between the bow-tie electrodes were selected to ensure a large nanowire-electrode contact area to allow for the successful integration of the nanowires in the THz detectors.

Fig.S2 illustrates the process flow (1-4) and the multi-stage transfer-printing mechanism (5, 6) implemented to integrate the nanowires in the THz detectors by means of nano-TP. Initially, a bespoke PDMS μ-stamp with a patterned 10 x 30 μm printing 'flat-tip' (*29*) was used to capture a selected nanowire from the intermediate PDMS surface. The μ-stamp (with the captured nanowire) was then moved over to a desired precise location in a 'bare' *z*-cut quartz substrate. The μ-stamp was controllably lowered down until surface contact between nanowire and substrate was produced to print the nanowire at the target position. As seen in Fig.S2(5), the transfer-printing process was iterated twice to integrate two separate nanowires adjacent to each other and with the same (parallel) orientation in the 'bare' *z*-cut quartz substrate. Fig.S2(6) shows in turn that after the electrodes were fabricated on top of the first set of transfer-printed nanowires, nano-TP processes were carried out again to integrate accurately two additional nanowires on top and across the other bow-tie electrode. This second set of adjacent nanowires was deliberately integrated with orthogonal orientation (as compared to that of the first nanowires set) to form the characteristic 'hashtag' design of the cross-nanowire THz detector. It is important to note here that the polymer PDMS μ-stamps are transparent; hence allowing the full visualization of the transfer-printing processes of the nanowires in real time. In addition, the nano-TP system has high-resolution translation stages and a large printing area capability yielding integration steps ranging from 1 mm to 100 nm over an area greater than 10 cm^2. These characteristics permit to accurately

identify the nanowires' capture and target release positions, introduce all needed positional adjustments to transfer-print the nanowires in the receiving surface to allow their precise integration (at adjacent locations and with specific orientations) both in the 'bare' *z*-cut quartz substrate or across the bow-tie electrodes forming the cross-nanowire THz detector design.

MM4. THz time-domain spectroscopy (THZ-TDS) system

A schematic diagram of the THz-TDS system setup used in this work is shown in Fig.S4. It was composed of a femtosecond laser, whose beam was split into two paths: one used to excite the emitter for pulsed THz generation and the other to excite the semiconductor detector for photocarrier generation. In detector operation, no external DC bias was required. Instead, the emitted THz pulse was focused on the photoexcited detector with aligned polarization across the detector electrodes, inducing a transient bias voltage across the electrodes and consequently a transient photocurrent in the detector that could be measured to recover the incident THz electric-field pulse. An interdigitated photoconductive emitter mounted in a motorized rotation stage was utilized in the system for generation of single-cycle linearly-polarized THz pulses. By rotating the emitter, the polarization of THz source could be rotated to any arbitrary angles (precision < 0.1°, from 0° to 360°, perpendicular to the propagation direction). In our system, the emitter angle was equal to the angle that the emitted THz pulse was polarized at, where 0° corresponded to the pulse polarized horizontally (with respective to the optical table) and 90° corresponded to the pulse polarized vertically. Our nanowire detector with two orthogonal detection channels was also aligned in the system, where one channel was orientated horizontally and the other vertically.

MM5. THz emitter characterization and system calibration

The polarization-variable THz-TDS system was realized by using a rotatable interdigitated photoconductive emitter (Tera-SED3, Laser Quantum UK, 3 mm × 3 mm) as shown in Fig.S4. A similar system based on the same emitter type has been reported in Ref (*12*), verifying its validity. For measurement accuracy, the optical pulse (on the emitter), emitter center and rotation axis are required to be perfectly aligned in the system, to ensure a minimal variation in the amplitude of the generated THz electric field with emitter rotation angle. As such, the emitter center was marked and carefully mounted in a rotation stage (where the emitter center is aligned to the rotation axis). The rotation stage (together with the emitter) was then loaded in a xy-stage, which was placed in the THz generation path of the system, allowing a precise alignment of the optical pulse to the emitter center.

In order to confirm the final alignment result, the resistance of the emitter under illumination (800 nm, fs-laser, 210 mW with 1 mm of beam spot size) as a function of emitter angle (from 0° to 180°) was measured (see Fig.S5A) showing an average resistance of 236.3 Ω and a variation of ~ 6%, indicating a well-aligned system (in its THz generation path). Following, a standard 0.2-mm thick (110) ZnTe crystal detector was used to align the system for its THz detection path, as well as to calibrate the system. Fig.S5B shows the (peak-to-peak) strength of the THz electric field measured from the ZnTe crystal detector as a function of emitter bias (when emitter is rotated at 0°). A fixed emitter bias of 14 V was then chosen for all the rest of the experiments in this work, as it was within the linear region of operation of our photoconductive emitter while enabling it

to produce strong enough THz electric fields for measurements with our nanowire detector.

Fig.S5C shows the measured (peak-to-peak) strength of THz electric field using the ZnTe crystal detector as a function of emitter angle, which follows a perfect cosine function, confirming the good system alignment in the THz detection path. In addition, a single bow-tie photoconductive detector based on an Fe^{+}-implanted InP substrate was fabricated and used for a fine adjustment of the system alignment (see Fig.S5D). The photoconductive detector shares the same operation mechanism as our nanowire detector and thus is a better reference to examine the cable connection and detector performance in comparison with our nanowire detector. The full spectral range of the incident THz spans from 0.1 to 3.0 THz (characterized by the two reference detectors).

MM6. Measurement setup

Two SR555 current preamplifiers and two model SR830 lock-in amplifiers were used in the experiments. For the lock-in amplifier, the time constant was set at 1 s with a choice of 24 dB/oct roll-off. For data acquisition, we set the acquisition bandwidth at 20 THz for all samples, and parameters such as scan speed and scan numbers are the same as well. To make sure the results from different types of detectors can be used for comparison, measurement setups and corresponding setting parameters were kept the same for measuring both nanowire and bulk photoconductive detectors. A femtosecond Ti: sapphire laser was used for THz generation and detection, which produces pulses at a center wavelength of 800 nm with a duration of ~35 fs and a repetition rate of 84.5 MHz. The pulsed laser was split into two beams. One (with an average power of ~180 mW and 1-mm beam spot size) was used to excite a photoconductive THz emitter that was biased with a square wave of ± 14 V amplitude at 10 kHz. The other beam was used to excite the detector sample at a fluence of 3.5 nJ/cm^2/pulse (with a beam spot size of 50 μm). The THz emitter, off-axis parabolic mirrors and THz detector were placed inside a vacuum chamber. All experiments were conducted under vacuum unless otherwise noted.

MM7. THz metamaterial design and fabrication

To demonstrate the applications of nanowire detectors for polarization-based THz-TDS measurements, a THz metamaterial composed of periodic arrays of twisted split-ring resonator (SRR) pairs was fabricated, and then characterized in our system using our nanowire detector (See Fig.3 in main text). This metamaterial is designed to induce a resonance splitting in the transmitted THz spectrum, accompanied by polarization conversion to the orthogonal direction. The metamaterial was patterned on a *z*-cut quartz substrate (10 mm × 10 mm × 0.5 mm) by EBL, followed by metal deposition of 10/300 nm Cr/Au (via thermal evaporation) and a lift-off process. The twisted SRR pair consists of two identical planar SRRs rotated by 90° with respect to each other. Detailed dimensions of the SRR pair can be found in Fig.S6. The SRR pair arrays occupied an area of 8 mm × 8 mm, much larger than the diameter of the incident THz beam (approximately 1 mm) on the metamaterial.

MM8. Finite-difference time-domain simulation

Simulations were carried out using finite-difference time-domain (FDTD) solver (Lumerical Inc) to examine (i) the two-orthogonal bow-tie electrode response to the

incident THz polarization and (ii) the coupling effect of the metamaterial to the incident THz radiation. The geometrical details of the two-orthogonal bow-tie electrode used in our nanowire detector is shown in Fig.S6A. The dimensions of the metamaterial unit cell used in this work are shown in Fig.S6B. In order to make the simulation environment closely match the experimental conditions, a custom-defined simulation source (a broadband pulsed THz 'Gaussian Source') with characteristics imported from the experimental data (e.g. temporal waveform profile) was utilized. A thickness of 4 μm was set for all gold patterns in simulation to avoid too-small mesh size in the z-direction. The default mesh size of our simulation was 2 μm (d*x*=d*y*=d*z*=2 μm). In the study of two-orthogonal bow-tie electrode, a PEC (perfect electrical conductor) material model was employed while a 200-nm mesh override region (d*x*=d*y*=d*z*=200 nm) was added to the electrode centre area (10 μm ×10 μm), allowing mapping of the detailed THz electric field distribution in this region (where the nanowires were located in the device). The simulated results are discussed in the main text.

Supplementary Text

ST1. Signal process technique

The current induced between the two contacts of a typical photoconductive antenna can be expressed as

$$I(\tau) \propto \int_{-\infty}^{+\infty} E_{(THz)}(t)\, \sigma(t-\tau) dt\,, \qquad (1)$$

where $E_{(THz)}(t)$ is the effective electric field of the THz transient at the photoconductive antenna and $\sigma(\tau)$ is the photoconductivity of the detection material as a function of time. When the detection material has a much longer charge-carrier lifetime (>100ps) than the duration of the THz transient, the conductivity can be approximated as a unit step function and the photoconductive detector is thereby categorized as an "integrating detector". In this case the photocurrent can be approximated by

$$I(\tau) \propto \int_{\tau}^{\infty} E_{(THz)}(t) dt\,. \qquad (2)$$

From equation (2), the THz electric field $E_{(THz)}(t)$ can be recovered from the $I(\tau)$ data by differentiation with respect to τ. More details can be found in Ref (*24*).

ST2. Noise performance

The chopping frequency of the emitter is a parameter that can have a significant influence on the response of the detector. In this work, we define signal as the peak-to-peak current on one time-domain scan, and noise as the standard deviation of the difference of two consecutive scans. The signal-to-noise ratio of our nanowire detector was measured as function of the emitter chopping frequency, which are shown in Fig.S7. The measured signal-to-noise ratio drops for low frequencies (<10 Hz). This drop could result from several factors, including 1/f noise and the poor response of the lock-in amplifier at very low frequencies. A gradient drop in the high frequency range (> 10 kHz) is also observed, which coincides very well with the gradient increasing of the input

impedance of the current preamplifier (SR555) used in this work, and therefore does not necessarily imply a real reduction of the signal to noise performance of the detector. The chopping frequency was set as 10 kHz for all measurements of nanowire detector reported in the main text to ensure the best signal-to-noise ratio performance.

ST3. Crosstalk issue

For comparison, we fabricated a multi-contact photoconductive antenna (on an Fe^+-implanted InP substrate), which has the same electrode structure as used in our nanowire detector. The Fe^+-implanted InP substrate acts as both the active material and device substrate. Since the gap of each bow-tie electrode is 4 μm in the detector that is much smaller than the optical beam spot size (50 μm) incident on the detector center. The region between neighboring electrodes will be inevitably photoexcited as well, causing current flows between the two-orthogonal bow-tie electrodes and thus crosstalk in between. Fig.S8 shows the crosstalk influence on the performance of this bulk reference detector. A difference in response current level can be clearly observed when the two orthogonal channels were measured simultaneously and separately. Most importantly, the angle-dependence response shapes of the two orthogonal channels seem to be rotated by 45° in comparison with the responses in our nanowire detector and are no longer able to be separated owing to the strong crosstalk.

The crosstalk issue makes it complex when defining and calculating the extinction ratio of the bulk multi-contact photoconductive antenna. In order to demonstrate the advantage of crosstalk free of our cross-nanowire detector, we compared its polarization selectivity with the other two types of conventional THz detectors (that measure one linear polarization): electro-optic sampling based on a 0.2 mm-thick (110) ZnTe crystal, and a single bow-tie photoconductive receiver fabricated on a bulk Fe^+-implanted InP substrate. The polarization selectivity of these conventional detectors was characterized using the same system and methodology with the recorded cross-polarized THz field extinction ratio being 580 and 900 for the ZnTe crystal and bulk bow-tie detector respectively (see Figs.S5C and S5D). This ratio was found to be 2500 for the horizontal channel (1440 for the vertical channel) for our cross-nanowire detector.

ST4. Polarization of the optical pulse exciting the detector

The nanowires are optically anisotropic to photoexcitation. Since the ultrafast optical pulse incident on the nanowire detector in this work was linearly polarized, it should be taken into account that the anisotropic absorption to the optical light relative to the nanowire orientation may cause the performance difference between the two orthogonal channels in our nanowire detector. We inserted a quarter waveplate to make the polarization of optical pulse on the detector changed from linear to circular and then repeated partial experiments. Fig.S9 presents the responses of our nanowire detector when it is excited by linearly polarized optical pulses and circularly polarized pulses. The horizontal channel performed a little better (by 10%) than the vertical channel in both cases, which means the absorption anisotropy to optical pulse in our nanowire detector is not the main reason causing the channel performance difference. Therefore, the nanowire-to-nanowire variation is most likely the reason for the difference, which can be mitigated by introducing a calibration (using a standard THz source) and normalization procedure for the time-domain data.

ST5. Raw data of the metamaterial measurements

A metamaterial, composed of periodic arrays of two edge-coupled orthogonal split-ring resonators (with gap orientation in the horizontal and vertical directions), was measured using our nanowire detector in the THz-TDS system. The emitter was rotated to provide linearly polarized pulses at 0° (horizontally). The THz pulse was measured after passing through the metamaterial. The coupling effect of the metamaterial to the incident THz pulse induced co- and cross- polarization components of the THz pulse in transmission direction, whose raw time-domain data are shown in Fig.S10.

ST6. Characterization of an x-cut quartz using nanowire detector

An *x*-cut quartz wafer with the ordinary and extraordinary axes in the horizontal and vertical directions was measured using our nanowire detector in the THz-TDS system. The emitter was rotated to provide linearly-polarized pulses at 45°. After the THz pulse passing through the quartz, the transmitted pulse was split by polarization into two directions (along the horizontal and vertical directions, respectively) with a 0.34-ps time delay in between (because of the birefringence of the *x*-cut quartz). Fig.S11A shows the raw time-domain data of the two split pulses. The projection plots in Fig.S11B and Fig.S11C show that the polarization of THz pulse changed from linear to elliptical (right handed) after propagating through the *x*-cut quartz. This quartz is designed to have a thickness of 1.55 mm and function as a quarter waveplate at 1 THz. As shown in Fig.S12A, after passing through the *x*-cut quartz, the THz pulse was straightforwardly measured by the two orthogonal detection channels of our detector. Fig.S12B presents the calculated values of the ordinary and extraordinary refractive indices of the *x*-cut quartz and its birefringence. The measured ellipticity as function of the frequency was also presented in Fig.S12B, indicating the electric field of the THz pulse become circular at 1 THz as expected. The characterization of a similar *x*-cut quartz has been reported in Ref (*13*), where a bulk three-contact photoconductive antenna was utilized showing consistent results. The previously reported work had to deal with the crosstalk issue (e.g. lots of workload on optical alignment on the detector) whereas our work was freed from it.

ST7. Bandwidth improvement

The useable bandwidth of any THz-TDS system depends on the intensity spectrum of the THz source and both the spectral response and sensitivity of the detector. Increasing the bandwidth of our cross-nanowire detector is of importance for its applications, which could allow additional vibrational and molecular modes to be quantified.

Here we focus on the detector's intrinsic spectral response characteristics. For a photoconductive THz detector (e.g. our semiconductor nanowire detector), its spectral response is a convolution determined by (1) the antenna response (e.g. field enhancement and resonant frequency) (2) the active material properties (e.g. photoconductivity rise time, carrier lifetime and mobility) and therefore, optimizations of the nanowire materials and antenna structures are important for improving the bandwidth of the detector itself.

Antenna Response: We performed FDTD simulations to examine the spectral response range, peak amplitude and sensitivity of the bow-tie antenna configuration used in the cross-nanowire detectors. The geometrical scaling of the bow-tie is expected to result in a broadband response to electromagnetic radiation. The response of the two-orthogonal bow-tie antenna to the spectral intensity of the THz source was simulated, and the results are shown in Fig.S13. The simulation confirms that the bow-tie antenna is a wideband antenna in THz regime, and is more sensitive at low-frequency, while showing a strong field enhancement to the incident THz field. Thus while emphasizing the response at low frequencies, it is still suitable for high frequency detection if provided the dynamic range of the detector is high enough.

Active Material Properties: The ideal active material for a high signal-to-noise photoconductive THz detector should possess (i) a high charge-carrier mobility and low dark resistivity to provide a high response current signal, and (ii) a short charge-carrier lifetime to reduce the detected noise. The bandwidth is determined by the risetime of photoconductivity after excitation with a femtosecond laser pulse and depends on the laser-pulse duration and electronic properties of the active material *(24)*. Fig.S1B shows a step function like onset of photoconductivity after laser excitation for the InP nanowires and a 35-fs laser reported in this work, indicating that fundamentally they should be suitable for extremely high bandwidth (>10THz) THz detectors. However, the ~2THz usable bandwidth of the cross-nanowire detector is primarily limited by the low spectral intensity above 1THz of the THz source used in this study (Fig.S13), and the signal-to-noise ratio of the detector itself. Nanowires can be designed and optimized to improve the signal-to-noise ratio. For example we previously proposed a modulation-doped InP nanowire structure in Ref (*19*), where we doped the InP nanowire at both ends during growth (maintaining the carrier mobility in the undoped segment while reducing the carrier lifetime due to doping). This modulation-doped nanowire was found to be highly light-sensitive, and produced excellent ohmic contacts in devices. This resulted in a 2.5-time improved signal-to-noise ratio and extended the useable detection bandwidth (up to 2.5 THz) as compared with the undoped InP nanowire detector (2 THz) used in this work.

Beyond a simple convolution of (1) antenna response and (2) nanowire properties, the impedance matching between nanowire and antenna is also important for optimizing dynamic range and hence useable bandwidth of cross nanowire detectors. The impedance of the nanowires can be altered by tuning the physical properties of the nanowires (diameter, length, doping, photoconductivity) and altering the number of parallel nanowires at the center of each antenna. Furthermore, the antenna impedance can also be optimized through changes to its design. All these areas will be the focus of future research and lead to higher performance cross-nanowire THz detectors.

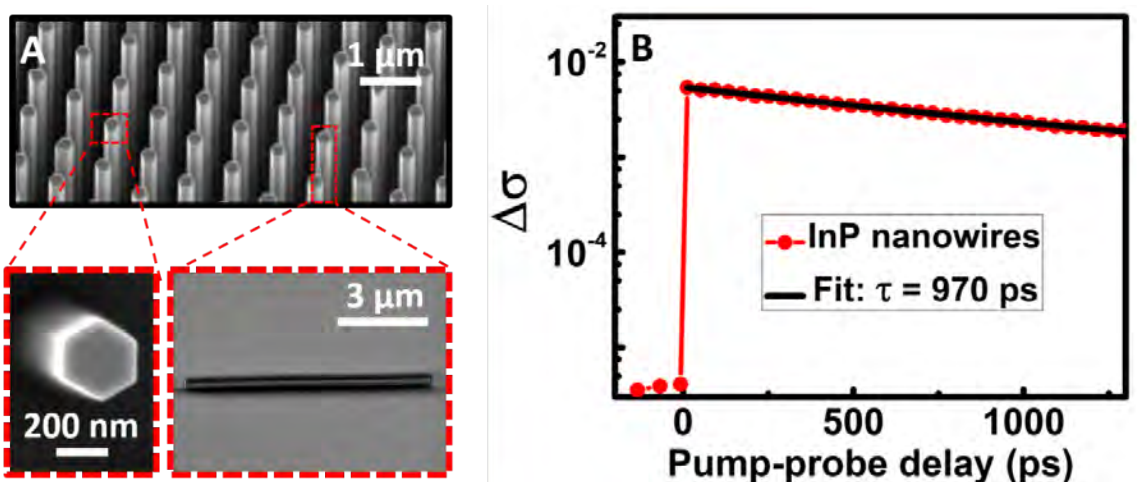

Fig. S1. Characterizations of the InP nanowires used in this study. (A) Scanning electron microscopy (SEM) images of an array of nanowires (top) and a single nanowire (bottom). **(B)** The rise and decay of photoconductivity of nanowires after photoexcitation by a 35-fs duration 800-nm wavelength laser pulse. The 970-ps photoconductivity lifetime of the nanowire indicates the nanowire detectors may be classified as "integrating" type.

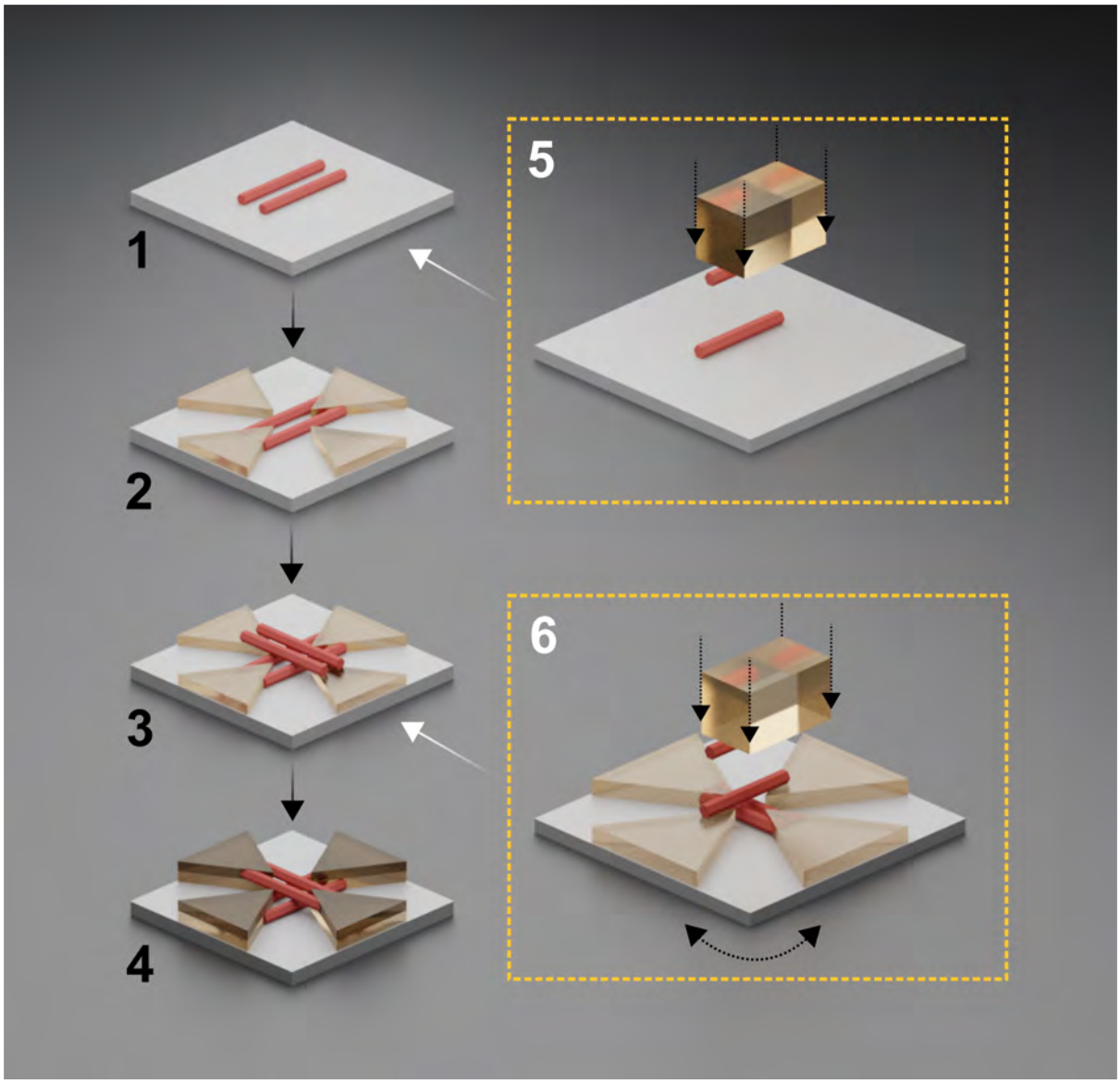

Fig. S2. Schematic illustration of the fabrication of a polarization-sensitive-cross-nanowire THz detector. (1-4) Process flow. (5, 6) Transfer printing of the nanowires in the initially 'bare' *z*-cut quartz substrate (5) and across the bow-tie electrodes (6) of the THz detector.

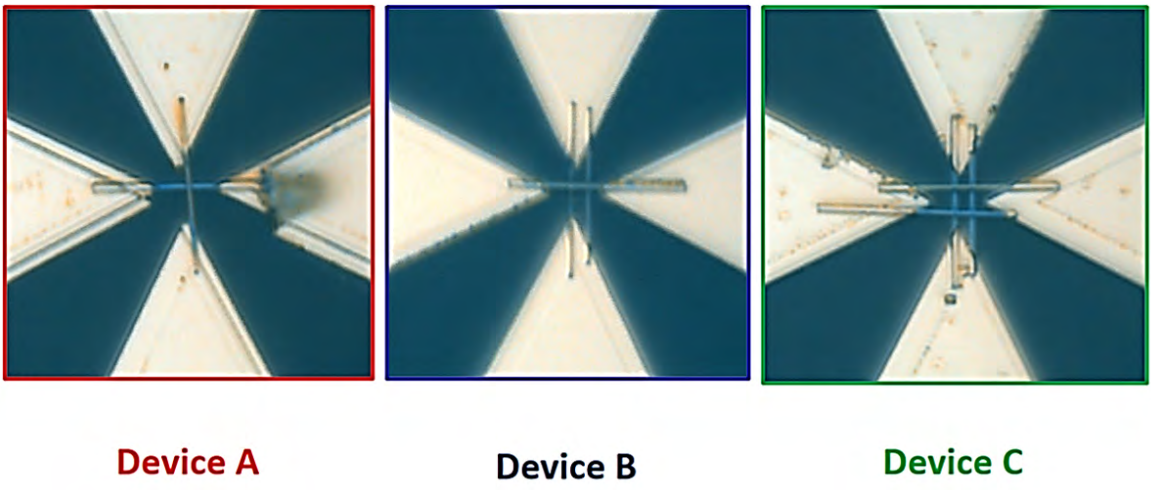

Fig. S3. Optical microscope images illustrating control of number of nanowires in the fabrication of polarization-sensitive-cross-nanowire THz detector. The gap size of each bow-tie electrode was 4 μm in device design.

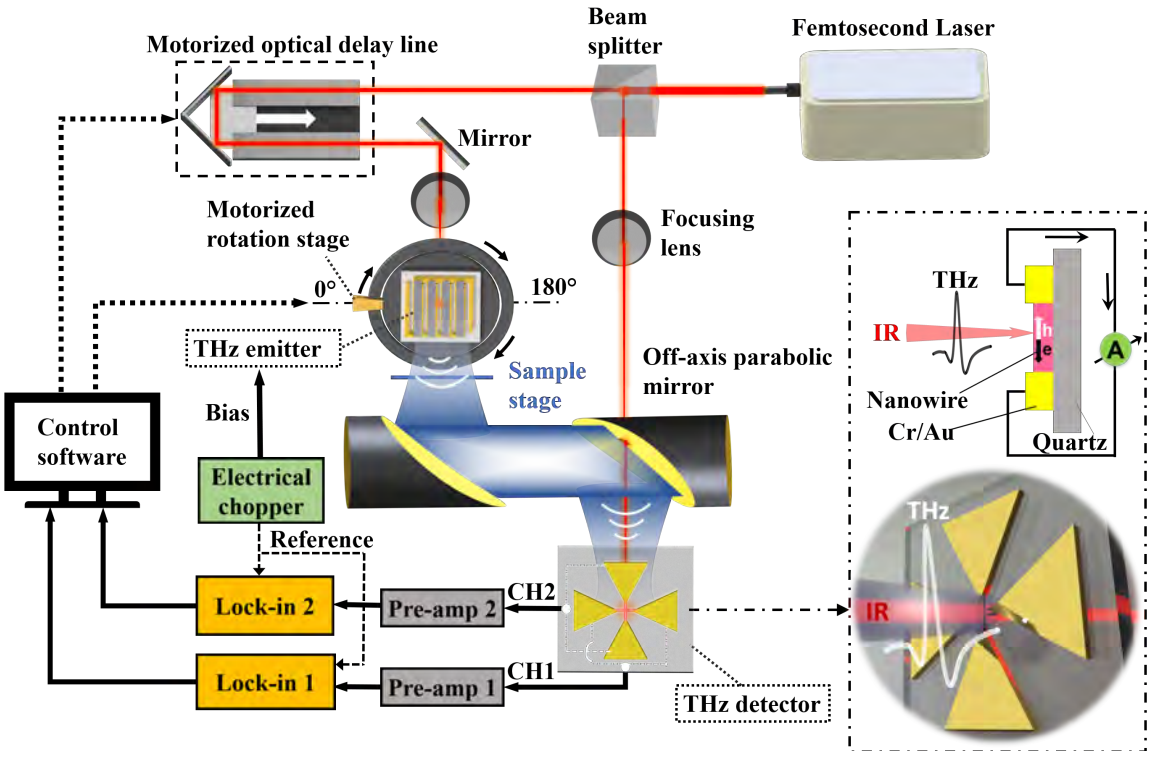

Fig. S4. Schematic diagram of the THz-TDS system used in this work. A part of the laser pulse was used to excite an interdigitated photoconductive THz emitter, which is biased with a square wave of ± 14V amplitude at 10 kHz. The emitter was mounted in a motorized rotation stage allowing to generate linearly polarized THz pulses that can be rotated to arbitrary angles. The insert image is a schematic illustration of the nanowire detector in operation.

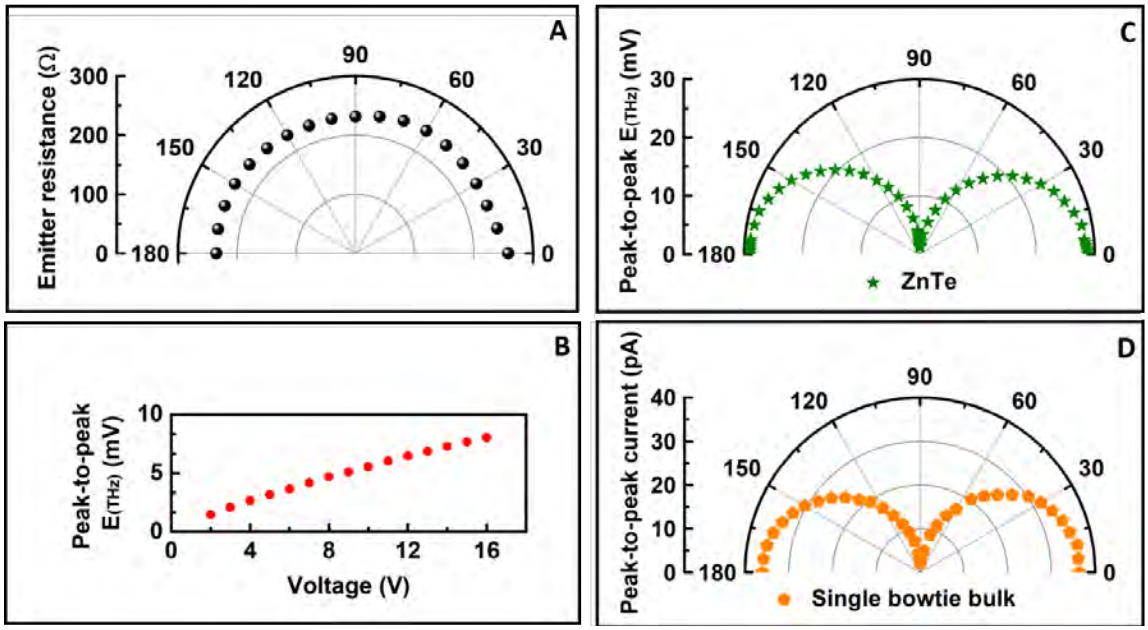

Fig. S5. Characterization of the THz-TDS system. (A) Dependence of the resistance of the interdigitated THz emitter on the emitter rotation angle. **(B)** Peak-to-peak amplitude of the THz electrical field, extracted from the time-domain signals detected by a standard (110) ZnTe crystal detector, as a function of applied bias voltage (when emitter rotation angle is set at 0°). **(C)** Dependence of the peak-to-peak amplitude of the THz electrical field detected by the ZnTe crystal detector on the emitter rotation angle when the applied bias was fixed at 14 V. **(D)** Dependence on the emitter rotation angle of the peak-to-peak current detected by a bulk single bow-tie photoconductive detector when the applied bias was fixed at 14 V.

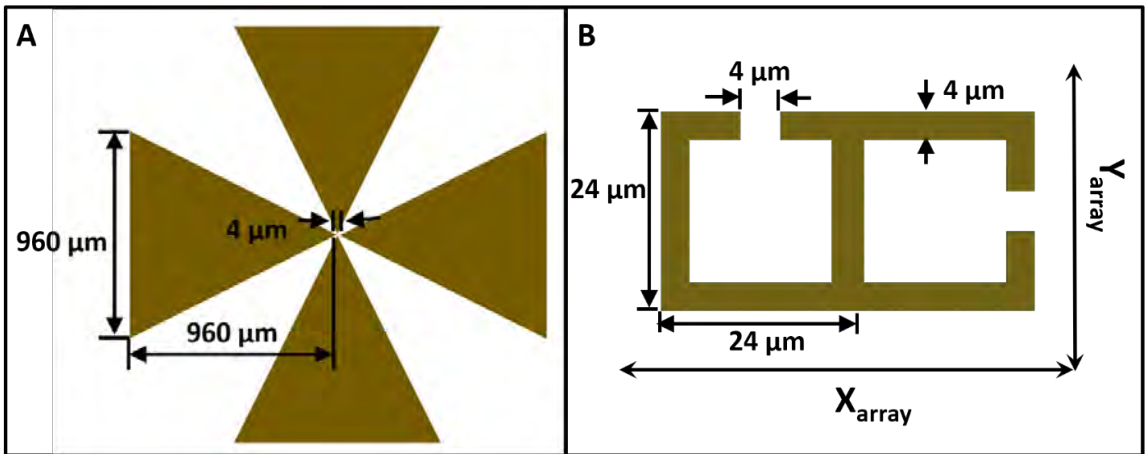

Fig. S6. Dimensions of important device geometries used in both the experiment and simulation. (A) two-orthogonal bow-tie electrode structure. **(B)** Unit cell of the metamaterial. The metamaterial is made of cell arrays with periods of X_{array} = 72 µm and Y_{array} = 36 µm in the *x* and *y* directions, respectively.

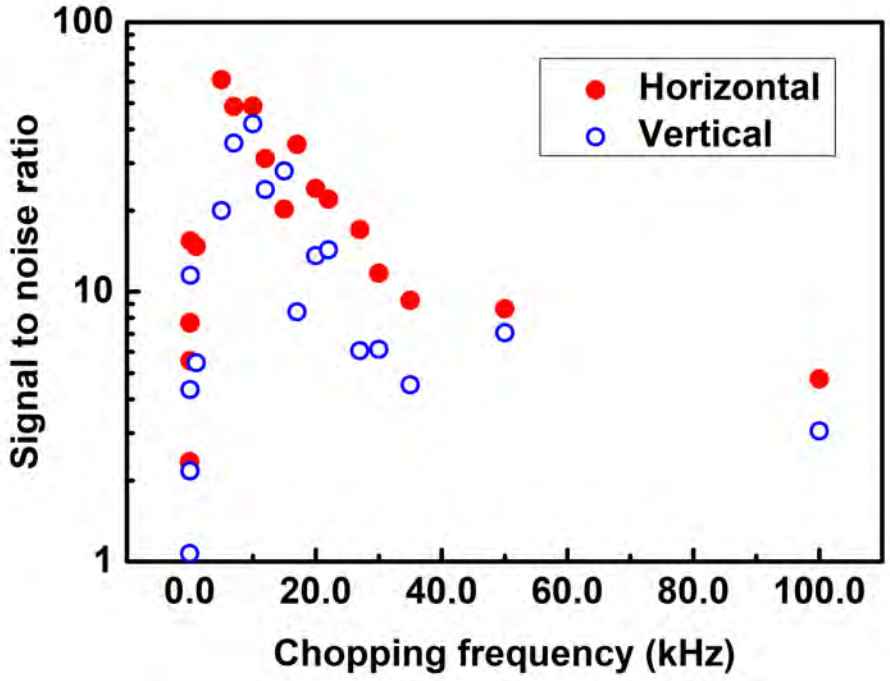

Fig. S7. Signal-to-noise ratio of the response of the polarization-sensitive-cross-nanowire THz detector as a function of chopping frequency. (Red): the horizontal channel. (Blue): the vertical channel.

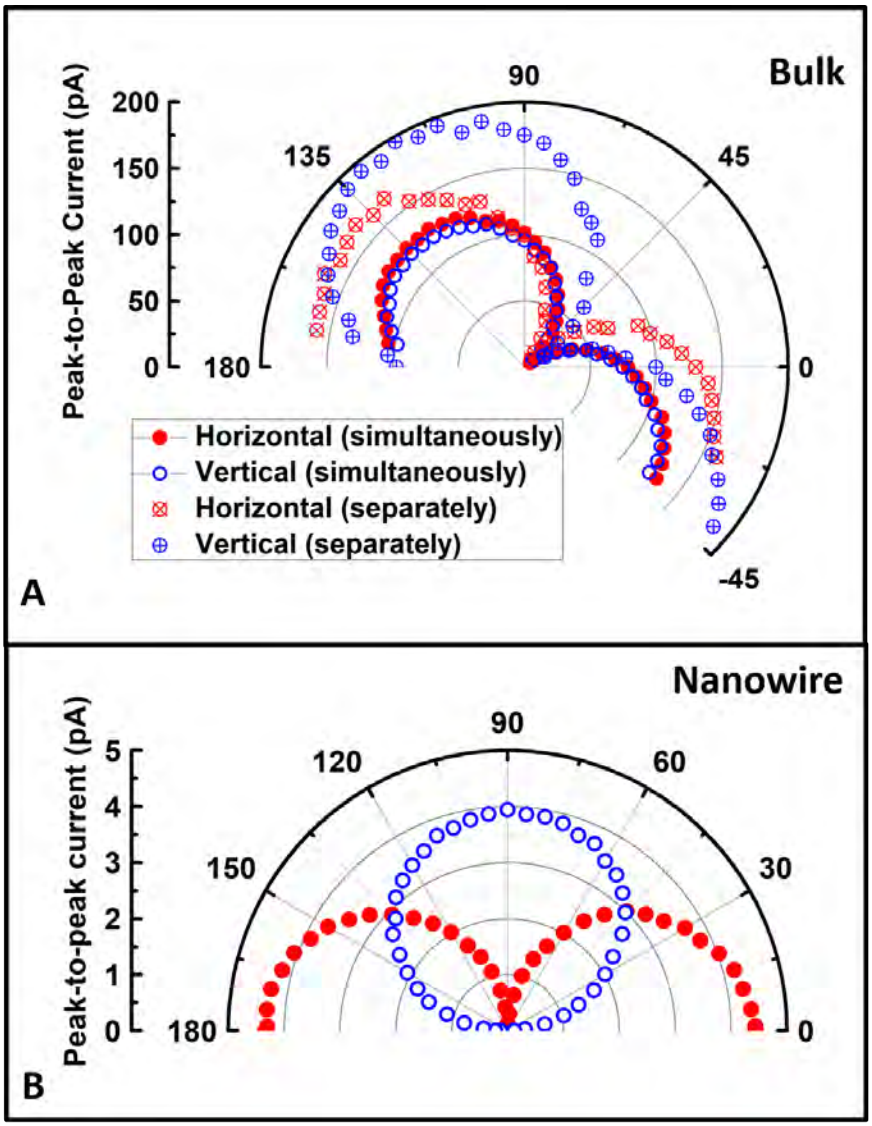

Fig. S8. Peak-to-peak current of the polarization-sensitive THz detector as a function of the incident THz polarization angle. (A) A bulk ion-implanted InP detector. **(B)** Nanowire detector. (Red): the horizontal channel. (Blue): the vertical channel. In the case of the bulk detector, (case 1) the two orthogonal channels were measured simultaneously (dots) and (case 2) the two orthogonal channels were measured separately (crossed dots).

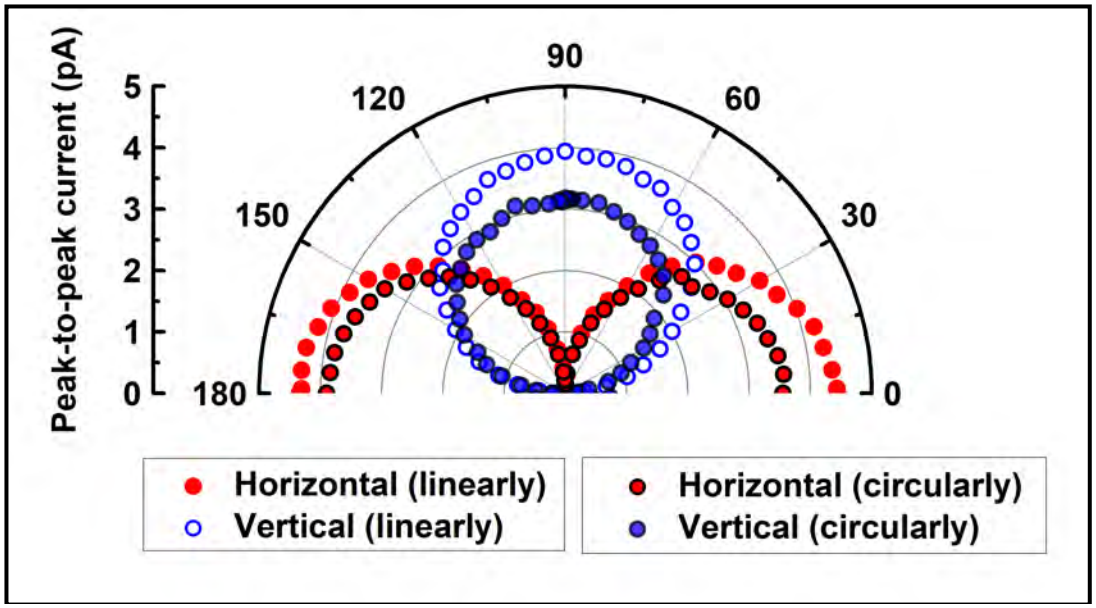

Fig. S9. Peak-to-peak current of the polarization-sensitive-cross-nanowire THz detector as a function of the incident THz polarization. (Red dot): the horizontal detection channel. (Blue dot): the vertical detection channel. Data dots without black outer shells refer to the case of linearly-polarized optical pulse excitation of the detector. Dot data with black outer shells refer to the case of circularly-polarized optical pulse excitation of the detector.

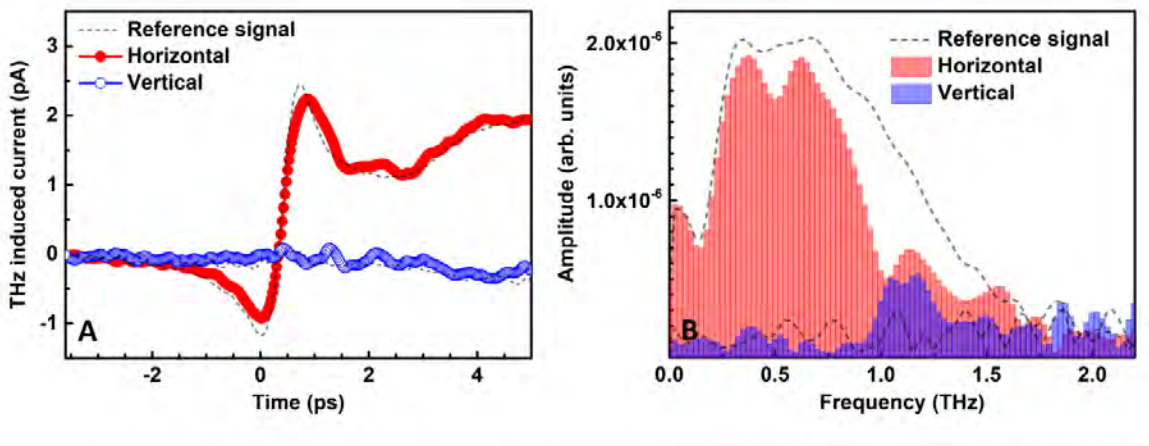

Fig. S10. Measurement of the metamaterial using the polarization-sensitive-cross-nanowire detector in THz-TDS. (A) Raw time-domain data. **(B)** Amplitude spectrum of the measured THz electric field. (Red): the horizontal detection channel. (Blue): the vertical detection channel. The dashed line indicates data without the metamaterial inserted in the system.

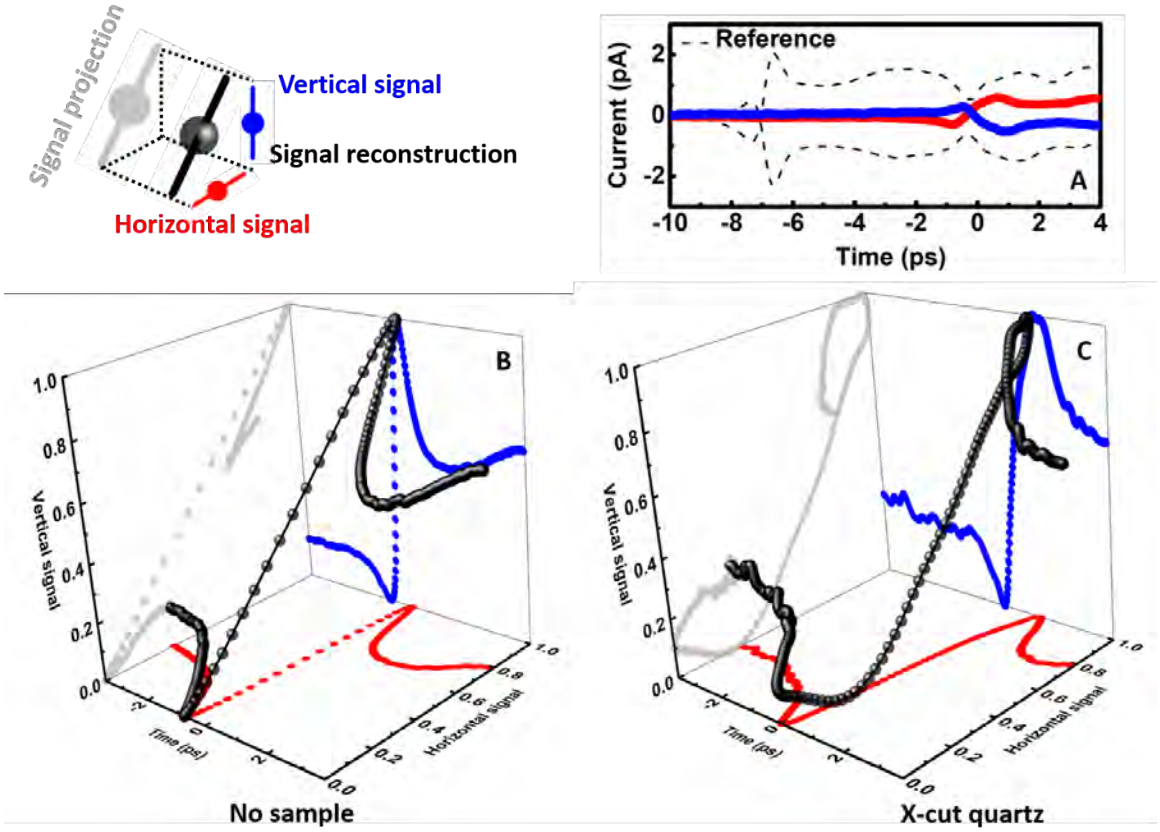

Fig. S11. Raw measurement data of the *x*-cut quartz wafer using the polarization-sensitive-cross-nanowire detector in THz-TDS. (A) Raw time-domain data. The dashed line indicates data without the *x*-cut quartz inserted in the system. **(B)-(C)** 3D projection plots of the (normalized) time-domain data corresponding to (A). (Red): the horizontal detection channel. (Blue): the vertical detection channel.

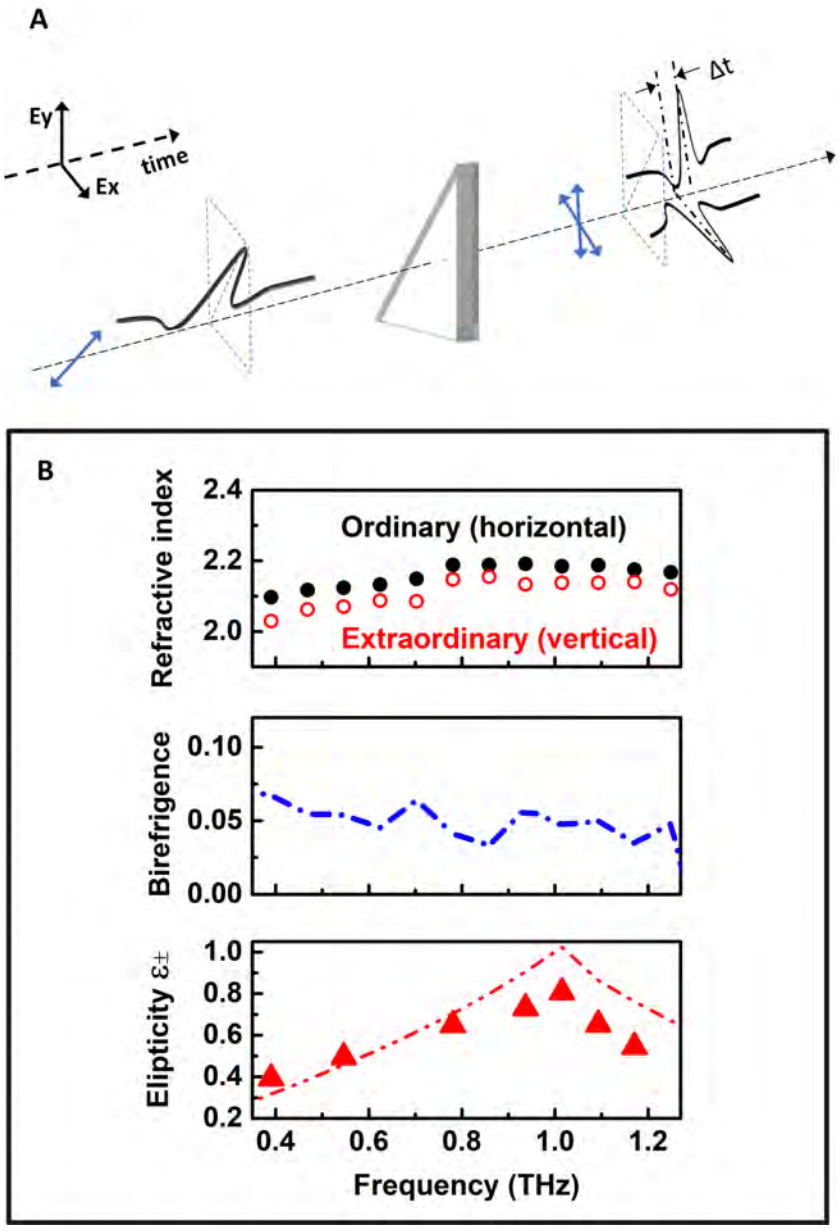

Fig. S12. Characterization of the *x*-cut quartz using the polarization-sensitive-cross-nanowire detector in THz-TDS. (A) Schematic representation of transmission measurement of an *x*-cut quartz wafer. **(B)** Birefringent properties of the *x*-cut quartz (top: ordinary and extraordinary refractive indices of quartz; middle: birefringence of quartz calculated form the refractive indices; bottom: ellipticity extracted from the transmitted two pulses). The dash line is the expected response as calculated for the waveplate.

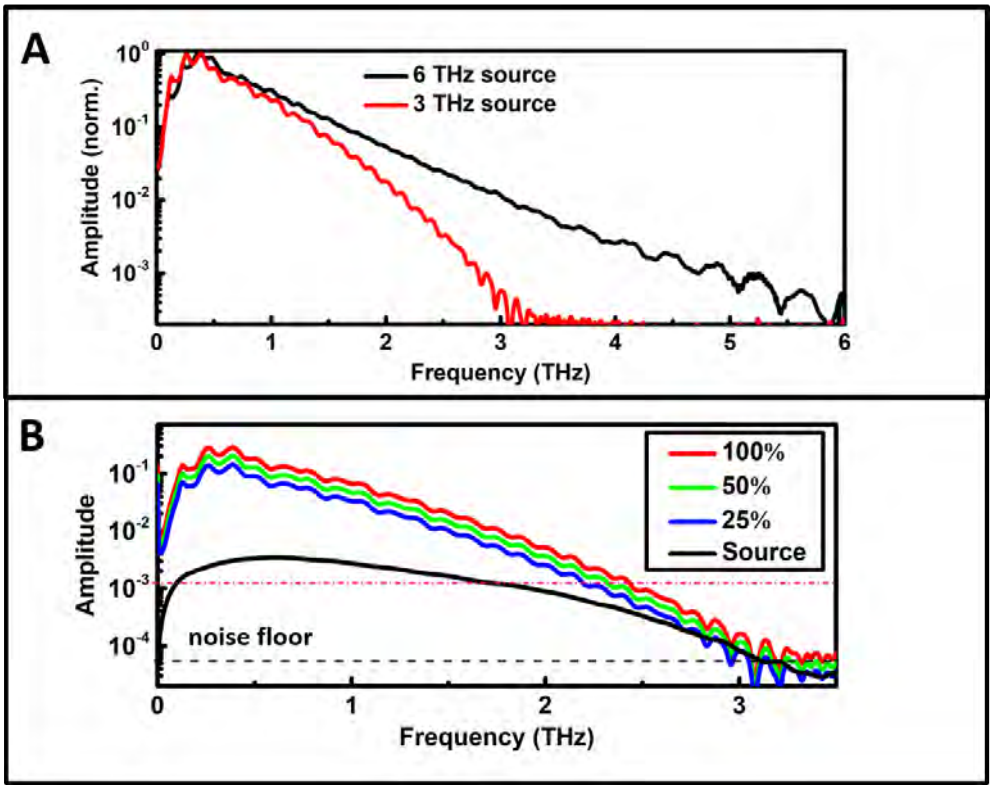

Fig. S13. Simulated spectral responses of the two-orthogonal bow-tie antenna in relation to the incident THz bandwidth (A) and power (B). The THz radiation is incident normal to the antenna surface and polarized horizontally. This plots only show the responses from the horizontal channel. The red dash-dot line is guide for the eye.

References:

1. S. Dhillon *et al.*, The 2017 terahertz science and technology roadmap. *Journal of Physics D: Applied Physics* **50**, 043001 (2017).
2. B. Ferguson, X. C. Zhang, Materials for terahertz science and technology. *Nature Materials* **1**, 26-33 (2002).
3. C. Riek *et al.*, Direct sampling of electric-field vacuum fluctuations. *Science* **350**, 420-423 (2015).
4. S. Schlauderer *et al.*, Temporal and spectral fingerprints of ultrafast all-coherent spin switching. *Nature* **569**, 383-387 (2019).
5. E. Castro-Camus, M. B. Johnston, Extraction of the anisotropic dielectric properties of materials from polarization-resolved terahertz time-domain spectra. *Journal of Optics A: Pure and Applied Optics* **11**, 105206 (2009).
6. D. M. Mittleman, J. Cunningham, M. C. Nuss, M. Geva, Noncontact semiconductor wafer characterization with the terahertz Hall effect. *Applied Physics Letters* **71**, 16-18 (1997).
7. K. N. Okada *et al.*, Terahertz spectroscopy on Faraday and Kerr rotations in a quantum anomalous Hall state. *Nature Communications* **7**, 12245 (2016).
8. W. Choi *et al.*, Terahertz circular dichroism spectroscopy of biomaterials enabled by kirigami polarization modulators. *Nature Materials* **18**, 820-826 (2019).
9. S. Watanabe, Terahertz polarization imaging and its applications. *Photonics* **5**, 58 (2018).
10. B. B. Hu, M. C. Nuss, Imaging with terahertz waves. *Optics Letters* **20**, 1716-1718 (1995).
11. Q. Chen, X. C. Zhang, Polarization modulation in optoelectronic generation and detection of terahertz beams. *Applied Physics Letters* **74**, 3435-3437 (1999).
12. C. D. W. Mosley, M. Failla, D. Prabhakaran, J. Lloyd-Hughes, Terahertz spectroscopy of anisotropic materials using beams with rotatable polarization. *Scientific Reports* **7**, 12337 (2017).
13. E. Castro-Camus *et al.*, An ion-implanted InP receiver for polarization resolved terahertz spectroscopy. *Optics Express* **15**, 7047-7057 (2007).
14. N. Nemoto, T. Higuchi, N. Kanda, K. Konishi, M. Kuwata-Gonokami, Highly precise and accurate terahertz polarization measurements based on electro-optic sampling with polarization modulation of probe pulses. *Optics Express* **22**, 17915-17929 (2014).
15. D. S. Bulgarevich *et al.*, A polarization-sensitive 4-contact detector for terahertz time-domain spectroscopy. *Optics Express* **22**, 10332-10340 (2014).
16. A. Hussain, S. R. Andrews, Ultrabroadband polarization analysis of terahertz pulses. *Optics Express* **16**, 7251-7257 (2008).
17. E. Castro-Camus *et al.*, Polarization-sensitive terahertz detection by multicontact photoconductive receivers. *Applied Physics Letters* **86**, 254102 (2005).
18. G. Niehues *et al.*, A matter of symmetry: terahertz polarization detection properties of a multi-contact photoconductive antenna evaluated by a response matrix analysis. *Optics Express* **23**, 16184-16195 (2015).
19. K. Peng *et al.*, Single n^+-i-n^+ InP nanowires for highly sensitive terahertz detection. *Nanotechnology* **28**, 125202 (2017).

20. K. Peng *et al.*, Broadband phase-sensitive single InP nanowire photoconductive terahertz detectors. *Nano Letters* **16**, 4925-4931 (2016).
21. K. Peng *et al.*, Single nanowire photoconductive terahertz detectors. *Nano Letters* **15**, 206-210 (2015).
22. S. A. Baig *et al.*, An ultrafast switchable terahertz polarization modulator based on III–V semiconductor nanowires. *Nano Letters* **17**, 2603-2610 (2017).
23. Z. Yang *et al.*, Single-nanowire spectrometers. *Science* **365**, 1017-1020 (2019).
24. E. Castro-Camus *et al.*, Photoconductive response correction for detectors of terahertz radiation. *Journal of Applied Physics* **104**, 053113 (2008).
25. T. J. Yen *et al.*, Terahertz magnetic response from artificial materials. *Science* **303**, 1494-1496 (2004).
26. C. Y. Li, C. C. Chang, Q. L. Zhou, C. L. Zhang, H. T. Chen, Resonance coupling and polarization conversion in terahertz metasurfaces with twisted split-ring resonator pairs. *Optics Express* **25**, 25842-25852 (2017).
27. Q. Gao *et al.*, Selective-area epitaxy of pure wurtzite InP nanowires: high quantum efficiency and room-temperature lasing. *Nano Letters* **14**, 5206-5211 (2014).
28. H. J. Joyce, J. L. Boland, C. L. Davies, S. A. Baig, M. B. Johnston, A review of the electrical properties of semiconductor nanowires: insights gained from terahertz conductivity spectroscopy. *Semiconductor Science and Technology* **31**, 103003 (2016).
29. B. Guilhabert *et al.*, Transfer printing of semiconductor nanowires with lasing emission for controllable nanophotonic device fabrication. *ACS Nano* **10**, 3951-3958 (2016).